



## Self-affine subglacial roughness: consequences for radar scattering and basal thaw discrimination in northern Greenland

Thomas M. Jordan<sup>1</sup>, Michael A. Cooper<sup>1</sup>, Dustin M. Schroeder<sup>2</sup>, Christopher N. Williams<sup>1</sup>, John D. Paden<sup>3</sup>, Martin J. Siegert<sup>4</sup>, and Jonathan L. Bamber<sup>1</sup>

<sup>1</sup>Bristol Glaciology Centre, School of Geographical Sciences, University of Bristol, Bristol, UK.

<sup>2</sup>Department of Geophysics, Stanford University, Stanford, California, USA.

<sup>3</sup>Center for Remote Sensing of Ice Sheets, University of Kansas, Lawrence, Kansas, USA.

<sup>4</sup>Grantham Institute and Department of Earth Science and Engineering, Imperial College, London, UK.

*Correspondence to:* T. M. Jordan (tom.jordan@bris.ac.uk).

**Abstract.** Subglacial roughness can be determined at variety of length scales from radio-echo sounding (RES) data; either via statistical analysis of along-track topography, or inferred from basal radar scattering. Past studies have demonstrated that subglacial terrain exhibits self-affine (fractal) scaling behaviour, where vertical roughness has a power-law relationship with the horizontal length scale.

- 5 A self-affine statistical framework, which enables a consistent integration of topographic roughness and radar scattering, has yet to be applied to RES. Here we do this for recent RES data from northern Greenland, and demonstrate that subglacial topography exhibits pronounced spatial variation in the Hurst (roughness power-law) exponent. A radar scattering model then enables us to explain how the Hurst exponent exerts strong topographic control upon radar scattering, which we map using the
- 10 waveform abruptness (pulse peakiness) parameter. Notably, lower abruptness (associated with diffuse scattering) occurs for regions with a higher Hurst exponent, and higher abruptness (associated with specular reflections) occurs for regions with a lower Hurst exponent. Finally, we compare the RES-derived data with an independent prediction for the subglacial thermal state of northern Greenland. This analysis shows that the majority of predicted thawed regions do not have the specular RES
- 15 scattering signature of deep subglacial lakes, and instead have a diffuse scattering signature.



## 1 Introduction

With the development of the newest generation of thermomechanical ice sheet models, there has been a growing awareness that better constraining the physical properties of the glacier bed is essential for improving their predictive capability (e.g. Price et al. (2011); Seroussi et al. (2013); Nowicki et al. (2013); Shannon et al. (2013); Sergienko et al. (2014); Ritz et al. (2015); Cornford et al. (2015)). Notably, the basal traction parameterisation - which encapsulates the thermal state, basal roughness, and lithology - is potentially the largest single geophysical uncertainty in projections of the response of ice sheets to climate change (Ritz et al., 2015). Distinction between frozen and thawed regions of the glacier bed is particularly important in constraining ice dynamics, since appreciable basal motion can only occur in regions where the glacier bed is wet (Seroussi et al., 2013; Macgregor et al., 2016). Airborne radio-echo sounding (RES) is the only existing remote sensing technique that can acquire bed data with sufficient spatial coverage to enable subglacial information to be obtained across the ice sheets (refer to Pritchard (2014) and Bamber et al. (2013a) for recent Antarctic and Greenland coverage maps). Often, however, there is great ambiguity in RES-derived subglacial information (Matsuoka, 2011), or RES-derived information is sub-optimal for direct applicability in ice sheet models (Wilkens et al., 2015). Subsequently, data analysis methods which seek to improve the clarity and glaciological utility of RES-derived subglacial information are undergoing a period of rapid development (e.g. Oswald and Gogineni (2008); Li et al. (2010); Fujita et al. (2012); Wolovick et al. (2013); Schroeder et al. (2013, 2016); Jordan et al. (2016)).

RES data-analysis methods for determining subglacial physical properties can be categorised in two ways; those which determine bulk properties (including the discrimination of basal water), and those which determine interfacial properties (subglacial roughness). Bulk material properties of the glacier bed can, in principle, be determined using the basal reflection coefficient (Bogorodsky et al., 1983; Peters et al., 2005; Jacobel et al., 2009; Schroeder et al., 2016). Performing basal reflection analysis on ice-sheet-wide scale is, however, greatly limited by uncertainty and spatial variation in englacial radar attenuation (Matsuoka, 2011; Matsuoka et al., 2012; Macgregor et al., 2012, 2015; Jordan et al., 2016). In contrast with bulk properties, subglacial roughness analysis methods are (near) independent of radar attenuation. Subglacial roughness can be determined either via statistical analysis of topography (typically spectral analysis) (Taylor et al., 2004; Siegert et al., 2005; Bingham and Siegert, 2009; Li et al., 2010; Rippin, 2013), or inferred from the electromagnetic scattering properties of the radar pulse (Oswald and Gogineni, 2008; Schroeder et al., 2014; Young et al., 2016)). Spectral analysis can provide valuable insight toward aspects past ice dynamics and landscape formation (Siegert et al., 2005; Bingham and Siegert, 2009; Rippin et al., 2014). However, since the technique is limited to investigating length scales greater than the horizontal resolution (typically  $\sim 30$  m or greater), the relevance of the method in informing contemporary basal sliding physics - which requires metre-scale roughness information (Weertman, 1957; Nye, 1970; Hubbard et al., 2000; Fowler, 2011) - remains unclear. Radar scattering is sensitive to the length scale of the



electromagnetic wave (Shepard and Campbell, 1999) ( $\sim 1$ -3 m in ice for the majority of airborne sounders), and can potentially reveal finer scale roughness information, including the geometry of subglacial hydrological systems (Oswald and Gogineni, 2008; Schroeder et al., 2013, 2015; Young et al., 2016). High reflection specularity, such as occurs for deep ( $> 10$  m) subglacial lakes (Oswald and Robin, 1973; Gorman and Siegert, 1999; Palmer et al., 2013), has been proposed to be a RES scattering signature that can aid in discrimination of thawed beds (Oswald and Gogineni, 2008, 2012).

Degrees of radar scattering can be mapped using either the waveform properties of the bed echo - e.g. the abruptness (pulse-peakiness) (Oswald and Gogineni, 2008), or by constraining the angular distribution of scattered energy - e.g. the specularity content (Schroeder et al., 2013; Young et al., 2016). Maps of both scattering parameters indicate defined spatial patterns, but, to date, have not been integrated with topographic-scale roughness analysis (horizontal length scales  $\sim 10$ s of metres and upwards). As such, there is a knowledge gap regarding the topographic control upon radar scattering. Observations indicate that subglacial roughness exhibits self-affine (fractal) scaling behaviour over length scales from  $\sim 10^{-3}$  m to  $\sim 10^2$  m (Hubbard et al., 2000; Macgregor et al., 2013). Self-affine scaling corresponds to when the vertical roughness increases at a fixed slower rate than the horizontal length scale, following a power-law relationship that is parameterised by the Hurst exponent (Malinverno, 1990; Shepard et al., 2001). It is observed for a wide variety of natural terrain (Smith, 2014), including: the surface of Mars (Orsei et al., 2003); volcanic lava (Morris et al., 2008); and alluvial channels (Robert, 1988). If widely present, the self-affinity of subglacial roughness poses a challenge for integrating topographic roughness with existing glacial radar scattering models (Berry, 1973; Peters et al., 2005; Macgregor et al., 2013; Schroeder et al., 2015). This is because these statistically stationary models assume that roughness is independent of horizontal length scale, and an artificial scale-separation between high frequency roughness and low frequency topography is present (Berry, 1973). Radar scattering models with non-stationary, self-affine statistics naturally incorporate the multi-scale dependence of roughness, and are in widespread use in other fields of radar geophysics (e.g. Shepard and Campbell (1999); Franceschetti et al. (1999); Campbell and Shepard (2003); Oleschko et al. (2003)).

In this study, we explore the connection between self-affine subglacial roughness and radar scattering for recently collected Operation Ice Bridge (OIB) RES data from the north western Greenland Ice Sheet (GrIS). We parameterise basal radar scattering using the waveform abruptness, which was previously incorporated in a basal thaw discrimination algorithm (Oswald and Gogineni, 2008, 2012). In their algorithm, high abruptness (specular reflections) is imposed as a necessary criteria for discrimination of basal thaw, and re-examining this algorithm in the context of self-affine statistics is a central goal. Firstly, we use examples from glacial topography to illustrate self-affine scaling and the role of the Hurst exponent (Sect. 2). We then describe along-track windowing methods that enable the spatial variation in topographic roughness and the Hurst exponent to be quantified from RES



90 data, along with the extraction of the waveform abruptness from the bed echo (Sect. 3). A self-affine  
 radar scattering model, adapted from planetary radar (Shepard and Campbell, 1999; Campbell and  
 Shepard, 2003), is then used to predict the relationship between the Hurst exponent and waveform  
 abruptness (Sect. 4). The radar scattering model predicts that regions with higher Hurst exponent  
 are associated with lower abruptness (diffuse scattering) and regions with lower Hurst exponent are  
 95 associated with higher abruptness (specular reflections), which enables us to explain the spatial re-  
 lationship between the Hurst exponent and waveform abruptness (Sect. 5.1, Sect. 5.2). Finally, we  
 analyse the statistics of our RES-derived data in predicted thawed and frozen regions of the glacier  
 bed (Sect. 5.3), using the recent basal thermal state synthesis mask in Macgregor et al. (2016). This  
 analysis demonstrates that the RES scattering signature in thawed regions is, overall, more diffuse  
 100 than in frozen regions, and indicates that the algorithm in Oswald and Gogineni (2008, 2012) is  
 likely to yield both false-positive and false-negative discrimination of basal thaw.

## 2 Self-affine subglacial roughness

### 2.1 Overview

Statistical methods to extract the Hurst exponent, and thus to quantify self-affine scaling behaviour,  
 105 are well established in the earth and planetary science literature (Malinverno, 1990; Shepard et al.,  
 2001; Kulatilake et al., 1998; Orosei et al., 2003). These space-domain methods extract the Hurst  
 exponent using the variogram (roughness verses profile length) and devioqram (roughness verses  
 horizontal lag). Our motivation for use of these methods, rather than the spectral (frequency-domain)  
 methods previously applied in studies of subglacial roughness (Taylor et al., 2004; Siegert et al.,  
 110 2005; Bingham and Siegert, 2009; Li et al., 2010; Rippin, 2013)), is that they better reveal self-  
 affine scaling behaviour (Turcotte, 1992; Shepard et al., 1995, 2001). Since the theory of self-affine  
 roughness and related space-domain methods are not widely discussed in the glaciological literature  
 - the only example being Macgregor et al. (2013) - we now provide a review of the key concepts.  
 In order to illustrate the validity of the model to subglacial terrain, we use RES data from northern  
 115 Greenland.

### 2.2 Interfacial roughness parameters

Topographic roughness can be measured by means of statistical parameters that are, in general,  
 a function of horizontal length scale (Shepard et al., 2001; Smith, 2014). Two different interfacial  
 roughness parameters - the root mean square (rms) height and rms deviation - are typically employed  
 120 in self-affine roughness statistics (Shepard et al., 2001). The rms height is given by

$$\xi(L) = \left[ \frac{1}{N-1} \sum_{i=1}^N (z(x_i) - \bar{z})^2 \right]^{\frac{1}{2}}, \quad (1)$$



where  $N$  is the number of sample points within the profile window of length  $L$ ,  $z(x_i)$  is the bed elevation at point  $x_i$ , and  $\bar{z}$  is the mean bed elevation of the profile.  $\xi$  represents the standard deviation in bed elevation about a mean surface, and is a Gaussian-distributed random variable. The rms deviation is given by

$$\nu(\Delta x) = \left[ \frac{1}{N} \sum_{i=1}^N [(z(x_i) - \bar{z}) - (z(x_i + \Delta x) - \bar{z})]^2 \right]^{\frac{1}{2}}, \quad (2)$$

where  $\Delta x$  is the horizontal step size (lag).  $\nu$  has a particular significance in the parameterisation of radar scattering models with self-affine statistics (Shepard and Campbell, 1999; Campbell and Shepard, 2003). We later demonstrate that  $\nu$ , rather than  $\xi$ , best enables a comparison to be drawn between topographic scale roughness and radar scattering from glacial RES. The rms slope, which is proportional the rms deviation, is also widely used in self-affine statistics, but we do not do so here.

### 2.3 Self-affine scaling behaviour and the role of the Hurst exponent

Self-affine scaling (which is a sub-class of fractal scaling behaviour) can be parameterised using the Hurst exponent,  $H$  (Malinverno, 1990; Shepard et al., 1995, 2001).  $H$  quantifies the rate at which roughness in the vertical direction increases relative to the horizontal length scale (and is defined for  $0 \leq H \leq 1$ ). For a self-affine interface the following power-law relationships hold:

$$\xi(L) = \xi(L_0) \left( \frac{L}{L_0} \right)^H, \quad (3)$$

and

$$\nu(\Delta x) = \nu(\Delta x_0) \left( \frac{\Delta x}{\Delta x_0} \right)^H, \quad (4)$$

where  $L_0$  is a reference profile length, and  $\Delta x_0$  is a reference horizontal lag (Shepard and Campbell, 1999; Shepard et al., 2001). Three limiting cases of self-affine scaling are typically discussed (Shepard and Campbell, 1999). Terrain with  $H=1$  (where the roughness in the vertical direction increases at the same rate as the horizontal length scale) is referred to as ‘self-similar’. Terrain with  $H=0.5$ , (where the roughness in the vertical direction increases with the square root of horizontal length scale) is referred to as ‘Brownian’. Terrain with  $H=0$  (where the roughness in the vertical direction is independent of horizontal length scale) is referred to as ‘stationary’. For a stationary ( $H=0$ ) interface it follows from Eq. (3) and Eq. (4) that  $\xi$  and  $\nu$  are independent of  $L$  and  $\Delta x$  respectively.

We will later demonstrate that subglacial terrain exhibits near-ubiquitous self-affine scaling behaviour with pronounced spatial structure and variation for  $H$ . Four examples of 10 km along-track bed elevation profiles which encompass the range of observed  $H$  values are shown in Fig. 1a, along with a zoom window to a 1 km track section in Fig. 1b. Clear differences are apparent between the different terrain examples. The black terrain and red terrain ( $H \approx 0.9$  and  $H \approx 0.7$ ) are between



Brownian and self-similar scaling, and exhibit ‘persistent’ trends where neighbouring points tend to  
 155 follow a general trend of increasing or decreasing elevation (Shepard and Campbell, 1999). A fea-  
 ture of terrain with these higher  $H$  values is that it tends to appear rough at larger length scales (low  
 frequency) and smooth at smaller length scales (high frequency). By contrast, the green terrain ( $H \approx$   
 $0.3$ ) is in the sub-Brownian scaling regime, and exhibits anti-persistent trends (where neighbouring  
 points tend to alternate between increasing and decreasing elevation). A feature of low  $H$  terrain  
 160 such as this is that it tends to have similar roughness across length scales. The blue terrain ( $H \approx 0.5$ )  
 is close to an ideal Brownian surface, and exhibits no overall persistent trends. The 10 km profile  
 windows in Fig. 1a represent the length of along-track data over which we make our estimates for  
 $H$  (see Sect. 3.2).

#### 2.4 Calculation of $H$ via the variogram and devioqram

165 In order to estimate  $H$ , and identify the length scale regime over which glacial terrain exhibits self-  
 affine behavior,  $\xi$  and  $\nu$  are plotted as a function of  $L$  and  $\Delta x$  respectively on double-logarithmic  
 scale plots; referred to as the variogram and devioqram respectively (Kulatilake et al., 1998; Shepard  
 et al., 2001). Variogram and devioqram plots for  $\xi(L)$  and  $\nu(\Delta x)$  for the four terrain examples in  
 Fig. 1 are shown in Fig. 2a and Fig. 2b respectively. It follows from Eq. (3) and Eq. (4) that, upon this  
 170 double-logarithmic scale, a straight line relationship is predicted for glacial terrain that is self-affine  
 with the gradient equal to  $H$ . In practice, a single self-affine relationship only holds over a limited  
 scale regime and a ‘break-point’ transition is often observed (Shepard et al., 2001). We describe how  
 we asses the break points for glacial terrain in Sect. 3.2, along with further details regarding the  
 application of the variogram and devioqram to along-track RES data. Fig. 2 clearly demonstrates the  
 175 significance of the Hurst exponent when assessing the relative roughness at different length scales,  
 with the green terrain ( $H \approx 0.3$ ) becoming rougher relative to the other terrain at the smaller scales.

The space-domain variogram and devioqram have an (approximate) correspondence to the frequency-  
 domain power spectrum (Turcotte, 1992; Shepard et al., 1995, 2001). In frequency-space, self-affine  
 scaling occurs when the power spectrum,  $S$ , has a relationship of the form  $S(k) \propto k^{-\beta}$  where  $k$  is  
 180 the spatial frequency and  $-\beta$  is the spectral slope. The relationship between  $\beta$  and  $H$  is dimension-  
 ally dependent, and for along-track data is given by  $H = \frac{1}{2}(\beta - 1)$  (Turcotte, 1992). Despite this  
 correspondence, the space-domain methods are recommended to estimate  $H$  as they are less noisy  
 and less likely to bias slope estimates than the power spectrum method (Shepard et al., 1995). The  
 study by Hubbard et al. (2000) observed self-affine scaling in the roughness power spectrum over  
 185 length scales from  $\sim 10^{-3}$ m to  $\sim 10$  m for different sites across recently deglaciated terrain in the  
 immediate foreground of Glacier de Tsanfleuron, Switzerland. Their range for measured values of  $\beta$   
 corresponds to  $2.27 < \beta < 2.48$ , which implies  $H \sim 0.7$ .



### 3 Analysis of RES data

#### 3.1 Ice penetrating radar system and data coverage

190 The airborne RES data used in this study were collected by the Center for Remote Sensing of Ice  
Sheets (CReSIS) within the Operation IceBridge (OIB) project, over the months March-May in  
years 2011 and 2014. For all measurements the radar instrument, the Multichannel Coherent Radar  
Depth Sounder (MCoRDS), was installed upon a NASA P-3B Orion aircraft. The sounder has a  
frequency range from 180 to 210 MHz, corresponding to a centre wavelength  $\sim 0.87$  m in ice.  
195 After accounting for pulse shaping and windowing, this results in a depth-range resolution in ice of  
 $\sim 4.3$  m (Rodríguez-Morales et al., 2014; Paden, 2015). For the flight lines considered, the along-  
track resolution after synthetic aperture radar (SAR) processing and multi-looking is  $\sim 30$  m with an  
along-track-sample spacing of  $\sim 15$  m (Gogineni et al., 2014). The 2011 and 2014 field seasons were  
used since they have a higher along-track resolution than other recent field seasons. Measurements  
200 from MCoRDS are supplied as data products with different levels of additional processing (Paden,  
2015). Level 2 data corresponds to ice thickness, ice surface, and bed elevation data, and is used to  
calculate topographic-scale roughness and the Hurst exponent (Sect. 3.2). Level 1B data corresponds  
to radar echo strength profiles, and is used to extract the waveform abruptness parameter from the  
bed echo (Sect. 3.3). Basal reflection values can also be extracted from Level 1B data. We do not do  
205 this here, since we do not wish to bias our interpretation due to uncertainty in radar attenuation.

The study focused upon data from north western Greenland, which encompasses measurements  
close to three deep ice cores: Camp Century, NEEM and NorthGRIP (Fig. 3). The coverage map  
is underlain by the predicted thermal state mask in Macgregor et al. (2016) (Fig. 11 in the original  
study), which we later use to perform statistical analysis of basal RES data in different thermal  
210 regions. This mask represents an up-to-date best estimate of thawed and frozen regions of the GrIS at  
a 5 km grid scale, and is based upon a trinary classification: likely thawed (red), likely frozen (blue),  
uncertain (grey). The mask was determined using four independent methods: thermomechanical  
modeling of basal temperature, basal melting inferred from radiostratigraphy, modeling of surface  
velocity, and surface texture observation. The mask is therefore independent of basal RES data, and  
215 hence our RES-derived data fields. Our reason for selection of this region is threefold: firstly, the  
region is similar to the RES basal thaw analysis by Oswald and Gogineni (2008, 2012); secondly,  
confidence regarding the basal thermal state is high in the vicinity of the ice cores; and thirdly, the  
data coverage for the 2011 and 2014 field seasons is of high density with a mixture of tracks in  
predicted thawed and frozen regions.

#### 220 3.2 Determination of topographic roughness and Hurst exponent from Level 2 data

The along-track spacing interval ( $\sim 15$  m) of the Level 2 data is half the horizontal resolution ( $\sim 30$  m), and the horizontal resolution represents the spacing at which bed elevation measurements



are considered as independent. Therefore, to remove local correlation bias, the Level 2 data were down-sampled, considering every second data point (corresponding to a  $\sim 30$  m along-track spacing). Each flight track was then divided into 10 km along-track profile windows, as shown in the examples in Fig. 1a. Each profile window was then linearly detrended, which acts to reduce bias from a greater sampling of higher frequency than low frequency signal components (Shepard et al., 2001). The windows overlap with a sample spacing of 1 km, with the centre of each window defined to be the point at which  $H$  and the roughness parameters are geolocated to. This ‘moving window’ approach was employed as it enables greater continuity in the estimates for  $H$ . Prior to estimating  $H$ ,  $\xi(L)$  and  $\nu(\Delta x)$  were computed following Eq. (1) and Eq. (2) respectively. These calculations used the ‘interleaving’ sampling method described in (Shepard et al., 2001), which enables all of the data points to be sampled effectively. Our windowing method is similar to that described in Orosei et al. (2003) for the self-affine characterisation of Martian topography, where a non-overlapping 30 km window was assumed. Our choice of 10 km for the profile window and 1 km for the effective resolution, represent a good trade-off between resolution and the smoothness of the derived data fields.

In this study we are interested in computing  $H$  at the length scale of the Fresnel zone ( $\sim 100$  m), since this enables the most accurate parameterisation of the radar scattering model described in Sect. 4. The focus on smaller length scales is also consistent with the recommendations in Shepard et al. (2001), due to the break point transitions that can occur in self-affine scaling behaviour. For the data we consider, the lower bounds of the horizontal length scales are  $\sim 90$  m for  $\xi(L)$  (since three elevation measurements are the minimum required to calculate  $\xi(L)$  using Eq. (1)) and  $\sim 30$  m for  $\nu(\Delta x)$ .  $\nu(\Delta x)$  therefore better enables the estimation of  $H$  at smaller length scales and we focused upon the devrogram method, Fig. 2b, (although we also used the variogram, Fig. 2a, for comparative purposes). Additionally, as suggested in Fig. 2 the relationships for  $\nu(\Delta x)$  are, in general, significantly smoother than  $\xi(L)$ . The upper length scales in the devrogram and variogram were set to be  $\Delta x=1$  km and  $L=1$  km respectively, which follows from the recommendation by Shepard et al. (2001) that at least 10 independent sections of track are used in the calculations. As shown in Fig. 2, the gradients ( $H$ ) were calculated using the first five data points (which, for the devrogram, is over the range  $\Delta x \sim 30$  m to  $\Delta x \sim 150$  m). Self-affine scaling behavior often extends beyond these length-scales and we estimated the break points for  $\xi(L)$  and  $\nu(\Delta x)$  using a segmented linear regression procedure. Briefly, this involved firstly calculating the gradient ( $H$ ) for the first five data points. Additional data points at increasing length scales were then added into each linear regression model, and the gradient was recalculated. A stopping criteria was then applied where if the new gradient was found to exceed a specified tolerance from the original estimate, then a break point was identified.



### 3.3 Determination of waveform abruptness from Level 1B data

The processing of the Level 1B data (the basal waveform) uses the procedure described in Jordan et al. (2016), which, in turn, is largely based upon Oswald and Gogineni (2008). Firstly, this involved performing an along-track average of the basal waveform, where adjacent basal waveforms are stacked about their peak power values and arithmetically averaged. This averaging approach is phase-incoherent and acts to smooth power fluctuations due to electromagnetic interference (Oswald and Gogineni, 2008). The size of the averaging window varies as a function of Fresnel zone radius, and subsequently each along-track averaged waveform corresponds to approximately a separately illuminated region of the glacier bed (see Jordan et al. (2016) for details). The degree of radar scattering is quantified using the waveform abruptness

$$A = \frac{P_{peak}}{P_{agg}}, \quad (5)$$

where  $P_{peak}$  is the peak power of the bed echo and  $P_{agg}$  is the aggregated power, which is calculated by a discrete summation of the bed echo power measurements in each depth range bin.  $P_{agg}$  was introduced by Oswald and Gogineni (2008) since, based upon energy conservation arguments, it is argued to be more directly related to the predicted (specular) reflection coefficients than equivalent peak power values. In radar altimetry, the waveform abruptness is commonly called ‘pulse peakiness’ (e.g. Peacock and Laxon (2004); Zygmuntowska et al. (2013)).

Fig. 4 shows three examples of basal waveforms, along with their corresponding  $A$  values. Observed values of  $A$  range from  $\sim 0.03$  to  $0.60$ , and in Sect. 4.3 we theoretically constrain the maximum value to be  $0.65$ . Higher  $A$  values are associated with specular reflections from smoother regions of the glacier bed, whilst lower  $A$  values are associated with diffuse reflections from rougher regions (Oswald and Gogineni, 2008). When calculating the summation for  $P_{agg}$ , a signal-noise-ratio threshold was implemented by testing for decay of the peak power to specified percentage above the noise floor. Thresholds of 1, 2, and 5 % were considered and 2 % was found to give the best coverage, whilst excluding obvious anomalies. Due to this quality filtering step there are therefore sometimes small gaps in the along-track  $A$  data.

The basal waveform (and hence the calculated values of  $A$ ), results from a superposition of along-track and cross track energy (Young et al., 2016). Subsequently, the anisotropy of radar scattering (and inferences regarding the anisotropy of subglacial roughness), is not explicitly revealed by  $A$ . Hence, the studies of Oswald and Gogineni (2008, 2012) treat  $A$  as an isotropic parameter, and we follow this approach here.



#### 4 Radar scattering model for self-affine roughness

##### 290 4.1 Overview

The waveform abruptness has previously been discussed without reference to roughness statistics, and here we do this using a self-affine radar scattering model. Radar scattering models from natural terrain fall into two different categories: ‘coherent’ which incorporate deterministic phase interference and ‘incoherent’ which incorporate random phase interference (Ulaby et al., 1982; Campbell and Shepard, 2003; Grima et al., 2014). Coherent scattering models are applicable where the reflecting region is orientated near-perpendicular to the incident pulse (the nadir regime) and the reflecting region is fairly smooth at the scale of the illuminating wavelength (Campbell and Shepard, 2003), which is normally assumed to be a good approximation for the RES of glacier beds (Peters et al., 2005; Macgregor et al., 2013; Schroeder et al., 2015).

300 Below we describe and adapt a coherent scattering model, first developed for the nadir regime of planetary radar sounding measurements, which incorporates self-affine roughness statistics (Shepard and Campbell, 1999; Campbell and Shepard, 2003). The model is parameterised using the Hurst exponent values derived from the subglacial topography (Sect. 3.2), and thus enables a connection to be made between the topographic roughness and radar scattering. Coherent scattering models can  
305 be used to model decrease in specularly reflected power as a function of rms roughness (Berry, 1973; Peters et al., 2005), and this is the central aspect of the model which we focus upon here. Specifically, we show that, under assumptions of energy conservation, this power decrease can be used to predict the relationship between the Hurst exponent and waveform abruptness.

##### 4.2 Modeling the coherent power

310 The physical assumptions behind the self-affine scattering model are summarised in Shepard and Campbell (1999). The central assumption that differentiates the model from coherent stationary ( $H=0$ ) models (Berry, 1973; Peters et al., 2005; Macgregor et al., 2013; Grima et al., 2014; Schroeder et al., 2015), is that the rms height increases as a function of radius,  $r$ , about any given point, following the self-affine relationship

$$315 \quad \xi(r) = \frac{1}{\sqrt{2}} \nu_\lambda \left( \frac{r}{\lambda} \right)^H, \quad (6)$$

where  $\nu_\lambda = \nu(\Delta x = \lambda)$  is the wavelength scale rms deviation. Equation (6) assumes radial isotropy for  $H$  and  $\xi$ , and, since we are focusing upon constraining the (near) isotropic abruptness parameter, is a justifiable approximation. The statistical distribution for  $\xi(r)$  is assumed to be Gaussian, which is similar to most  $H=0$  models (but with an additional radial dependence.) Via  $\nu_\lambda$ , the self-affine model  
320 is explicitly formulated with respect to the horizontal scale of rms roughness. The radio wavelength of MCoRDS in ice is  $\sim 0.87$  m (Paden, 2015), and hence wavelength scale rms deviation is approximately equivalent to metre scale rms deviation. An unavoidable caveat to the parameterisation of the



radar scattering model using Eq. (6) is that the  $H$  values derived from the topography (length scale  $\sim 30$ -150 m) are extrapolated downwards to the wavelength scale.

325 An expression for the radar backscatter coefficient (radar cross-section per unit area) is then derived by considering a phase variation,  $\frac{4\pi\xi(r)}{\lambda}$ , integrated across the Fresnel zone (Shepard and Campbell, 1999; Campbell and Shepard, 2003). For nadir reflection the radar backscatter coefficient is given by

$$\sigma_0 = \frac{16\pi^2 R_e^2}{\hat{r}_{max}^2} \left( \int_0^{\hat{r}_{max}} \exp \left[ -\frac{4\pi^2}{\lambda^2} \nu_\lambda^2 \hat{r}^2 H \right] \hat{r} d\hat{r} \right)^2, \quad (7)$$

330 where  $\hat{r} = \frac{r}{\lambda}$  is the wavelength-scaled radius,  $\hat{r}_{max}$  is the wavelength-scaled radius of the illuminated area (the Fresnel zone), and  $R_e$  is the reflection coefficient for the electric field (Campbell and Shepard, 2003). The coherent power,  $P$ , can then be obtained by dividing Eq. (7) by  $4\pi^2 \hat{r}_{max}^2$  (a geometric factor which follows from the backscatter coefficient of a flat conducting plate (Ulaby et al., 1982)) to obtain

$$335 \quad P = \frac{4R_e^2}{\hat{r}_{max}^4} \left( \int_0^{\hat{r}_{max}} \exp \left[ -\frac{4\pi^2}{\lambda^2} \nu_\lambda^2 \hat{r}^2 H \right] \hat{r} d\hat{r} \right)^2. \quad (8)$$

For the case where  $H=0$ ,  $\xi(r)$  in Eq. (6) is independent of radius. It follows that  $\xi^2 = \frac{1}{2}\nu_\lambda^2$  and the exponent in Eq. (8) is also independent of radius which gives

$$P = R_e^2 \exp \left( -\frac{16\pi^2}{\lambda^2} \xi^2 \right). \quad (9)$$

340 Equation (9) is the same power decay formula as coherent  $H=0$  models (Peters et al., 2005; Macgregor et al., 2013; Grima et al., 2014; Schroeder et al., 2015), where it is sometimes multiplied by a first order Bessel function (which enables some of the incoherent energy contribution to be captured (Macgregor et al., 2013)). Thus the stationary limit of the model that we use is consistent with previous glacial basal scattering models. It is clear that the coherent power for the self-affine model, Eq. (8), has two roughness degrees of freedom:  $H$  and  $\nu_\lambda$ , which can be conceptually related to the  
 345 gradient and the intercept of the devioqram (Fig. 2). This contrasts with the stationary model, Eq. (9), which has one degree of freedom:  $\xi$ .

### 4.3 Relationship between the Hurst exponent and waveform abruptness

The utility of the waveform abruptness in quantifying different degrees of scattering, rests upon the assumption that the majority of the overall energy is contained within the echo envelope (Oswald and  
 350 Gogineni, 2008). In other words, it is assumed that, for reflection from the same bulk material, the aggregated/integrated power from a rough interface ( $\nu_\lambda > 0$ ) is equivalent to the peak power from a given smooth interface: i.e.  $P_{agg} \approx P(\nu_\lambda = 0)$ . This energy equivalence was demonstrated to hold well for the waveform processing procedure and Greenland RES systems by Oswald and Gogineni



(2008). It follows from this energy equivalence that the abruptness,  $A$ , can be expressed in terms of  
 355 the coherent power, Eq. (8), as

$$A = \frac{P_{peak}}{P_{agg}} = C \frac{P(\nu_\lambda)}{P(\nu_\lambda = 0)}, \quad (10)$$

where  $C$  is a proportionality constant that corresponds to the theoretical maximum abruptness value  
 which occurs when the radar pulse is specularly reflected and  $P_{agg} = P_{peak}$ . For specular reflection  
 the pulse is the shape of compressed chirp with the pulse width determined by the signal bandwidth,  
 360 and  $C$  can be estimated from the number of range cells which fit in the depth-range resolution ( $\sim$   
 0.65). Finally, substituting Eq. (8) into Eq. (10) gives

$$A = \frac{4C}{\hat{r}_{max}^4} \left( \int_0^{\hat{r}_{max}} \exp \left[ -\frac{4\pi^2}{\lambda^2} \nu_\lambda^2 \hat{r}^2 H \right] \hat{r} d\hat{r} \right)^2. \quad (11)$$

As is the case for  $P$  in Eq. (8), Eq. (11) has two roughness degrees of freedom:  $H$  and  $\nu_\lambda$ . Shepard  
 and Campbell (1999) note that the primary dependence for  $P$ , (and hence  $A$ ), is upon  $H$ ; with a  
 365 weaker secondary dependence upon  $\nu_\lambda$ . In order to illustrate this dependency, we firstly consider the  
 relationship between  $A$  and  $H$  for fixed  $\nu_\lambda$  (Fig. 5a), and secondly the relationship between  $A$  and  
 $\nu_\lambda$  for fixed  $H$  (Fig. 5b). Fig. 5a demonstrates that higher values of  $\nu_\lambda$  (the black curve), result in  
 negligible  $A$  for all but the lowest values of  $H$ . Intermediate values of  $\nu_\lambda$  (the red and blue curves),  
 exhibit a sharp transition from higher to lower values of  $A$  as  $H$  increases. Low  $\nu_\lambda$  (the green curve)  
 370 has high  $A$  for all  $H$ . Fig. 5b demonstrates a monotonic decrease in  $A$  with  $\nu_\lambda$  for each value of  $H$ ,  
 with the decay length decreasing rapidly with increasing  $H$ .

The physical explanation for the strong dependence of the coherent power upon  $H$ , and the rela-  
 tionships which we observe in Fig. 5, is discussed by Shepard and Campbell (1999) and Campbell  
 and Shepard (2003). It relates to the fact that significant coherent returns can only occur from annu-  
 375 lar regions where  $\xi(r) < \left(\frac{\lambda}{8}\right)$  (the Rayleigh criterion). It follows from Eq. (6) that high values of  $H$   
 lead to a rapid increase in roughness with radius that rapidly exceeds this threshold. Subsequently,  
 for high  $H$  interfaces, the roughness at the wavelength scale,  $\nu_\lambda$ , must be a couple orders of mag-  
 nitude smaller than the Rayleigh criterion to enable significant coherent returns (i.e. non-negligible  
 $A$ ). The curves in Fig. 5 assume  $\hat{r}_{max}=100$  (corresponding to a Fresnel zone radius  $\sim 115$  m for  
 380 the ice wavelength  $\sim 0.87$  m). In general, the relationships in Fig. 5 are insensitive to this choice of  
 radius. This is because the radii of the coherent annular regions are typically significantly less than  
 the Fresnel zone, and thus act as the dominant length scale for the integration limit in Eq. (11).

## 5 Results

Firstly, we describe maps for the Hurst exponent, rms deviation (topographic roughness), and the  
 385 waveform abruptness (radar scattering) in northern Greenland (Sect. 5.1). Secondly, we compare the  
 observed relationship between the Hurst exponent and waveform abruptness with the predictions of



the self-affine radar scattering model (Sect. 5.2). Thirdly, we perform a statistical analysis of the Hurst exponent and the waveform abruptness in predicted thawed and frozen regions of the glacier bed corresponding to the predicted thermal state mask in Macgregor et al. (2016) (Sect. 5.3). Since  
390 our primary focus is exploring the relationship between the Hurst exponent and waveform abruptness (which we demonstrate to be near isotropic), we choose not to investigate roughness anisotropy in detail.

### 5.1 Maps for Hurst exponent, topographic-scale roughness, and waveform abruptness

A map for  $H$ , overlaid by the frozen-thawed mask, for the north western GrIS is shown in Fig.  
395 6a. The calculations use the devioqram for  $\nu(\Delta x)$ , and  $H$  is estimated over the horizontal length scale  $\Delta x \sim 30$ -150 m. In general, higher values of  $H$  occur toward the margins of the ice sheet (generally, but not exclusively, thawed regions) and lower values toward the interior (generally, but not exclusively, frozen regions). The mean  $r^2$  value for the devioqram linear regression fits was  $\sim 0.99$ , indicating a very high overall correlation of the linear model. These correlation fits are,  
400 however, probably artificially high due to the smoothing of the data that occurs when applying the windowing and repeated sampling approach described in Sect. 3.2, and are unlikely to represent the true accuracy of the RES-derived data. There are clearly some discontinuities in the along-track maps in 6a which are likely explained by either anisotropy in  $H$  (due to underlying roughness anisotropy); or due the self-affine terrain model breaking down in certain regions (e.g. a sharp terrain discontinuity  
405 such as a subglacial cliff).

Calculation of  $H$  was also performed using the variogram for  $\xi(L)$ , over the length scale  $L \sim 90$ m to  $L \sim 210$  m. The map for  $H(\xi(L))$  (not shown) has the same overall spatial distribution as in Fig. 6a but with greater high frequency noise apparent and a correspondingly lower mean  $r^2$  value ( $\sim 0.96$ ). Due to the differing length scales in the  $H(\xi(L))$  and  $H(\nu(\Delta x))$  estimates, direct cross-over  
410 analysis is not possible. However, differencing the estimates as  $H(\nu(\Delta x)) - H(\xi(L))$ , gives a small mean bias of -0.026 and a cross-over standard deviation of 0.10 (10% of the parameter range). This is likely to better represent the accuracy of the data than the linear model fit uncertainties. Repeat cross-over analysis using different profile window sizes for the processing in Sect. 3.2 (e.g. 15 km) confirms that 0.10 serves a reasonable estimate for uncertainty of  $H$ .

415 Maps for  $\nu(\Delta x=30$  m) (the horizontal resolution and the smallest length scale in the devioqram calculation for  $H$ ),  $\nu(\Delta x=150$  m) (slightly larger than the typical size of the Fresnel zone, and the largest length scale used in the devioqram) are shown in Fig. 6b and c respectively. The spatial distributions indicate that, at each respective length scale, relatively rough terrain is present toward the margins of the ice sheet (typically, but not exclusively, thawed regions), and relatively smooth  
420 terrain is present in the interior (typically, but not exclusively, frozen regions). Despite the clear spatial variation in  $H$  in Fig. 6a, the overall spatial distribution for  $\nu(\Delta x=30$  m) and  $\nu(\Delta x=150$  m) are remarkably similar. Thus, from a purely visual inspection of the topographic-scale roughness,



the pronounced spatial variation in self-affine scaling behaviour is not apparent. As with the map for  $H$ , the rms deviation data at some of the flight track intersections is suggestive that a degree of roughness anisotropy is present.

A map for  $A$  is shown Fig. 6d. There is a high degree of spatial structure, with near-continuous regions of higher  $A$  (specular reflections) present in parts of the frozen interior, and also toward the north western margin near Camp Century. Values of  $A$  range from  $\sim 0.03$  to  $0.60$  which is in agreement with our theoretically constrained maximum abruptness value of  $0.65$  determined in Sect. 4. Cross-over analysis from flight track intersections indicates that variation in  $A$  is  $\sim 0.05$  (less than 10% the parameter range). This variation is approximately the same for inter- and intra- field campaign cross-over analysis (although this is to be expected since the radar systems are similar). This variation also incorporates any minor variation due to anisotropy, and confirms that  $A$  is near-isotropic. Similar continuous regions of high abruptness in the northern interior were observed by Oswald and Gogineni (2008, 2012).

As part of the analysis we also considered estimation of the breakpoint transitions for  $\xi(L)$  and  $\nu(\Delta x)$  using the segmented linear regression procedure described Sect. 3.2. The exact values of the breakpoints depend upon how strict the stopping criteria is, so here we just discuss some general trends. Firstly, the self-affine scaling relationships often extend over a much greater length scale than the upper length scale used in the  $H$  estimates (often over  $500$  m as occurs in Fig. 2). Secondly, as is also the case in Fig. 2, the breakpoints for  $\nu(\Delta x)$  generally occur at greater length scales than for  $\xi(L)$ . Thirdly, the break points for both  $\nu(\Delta x)$  and  $\xi(L)$  tend to be greater toward the ice sheet margins.

## 5.2 Observed relationship between Hurst exponent and waveform abruptness

The total frequency distribution for  $H$ , corresponding to the along-track calculations in Fig. 6a, is shown in Fig. 7a. The distribution is divided into three categories: (i)  $H > 0.75$  ('High'  $H$ ); (ii)  $0.5 < H \leq 0.75$  ('Medium'  $H$ ); (iii)  $H \leq 0.5$  ('Low'  $H$ ), which we later employ in comparative analysis with the waveform abruptness. Approximately 0.1% of the  $H$  estimates are  $> 1$  and none of the  $H$  estimates are  $< 0$ , representing near-ubiquitous self-affine scaling behaviour, ( $0 < H < 1$ ). A overall negative skew for the distribution of  $H$  is observed with a mean value of  $0.65$ , indicating that the majority of the subglacial terrain along the flight tracks lies between Brownian ( $H=0.5$ ) and self-similar ( $H=1$ ) scaling regimes. The spatial coverage of the radar flight tracks in Fig. 6a is, however, more comprehensive in regions of higher  $H$ . Thus the mean value and skew of  $H$  in Fig. 7a are likely overestimates and underestimates of true (equal area) averaged values for the region of the northern GrIS in Fig. 3.

The self-affine coherent scattering model, Sect. 4, predicts that there are two roughness degrees of freedom that control  $A$ :  $H$  (the primary control) and  $\nu_\lambda$  (the secondary control). Given the primary dependence of  $A$  upon  $H$ , a natural starting point is to compare the model predictions with the



observed relationship between  $A$  and  $H$ . Based upon the assumption that  $\nu_\lambda$  (which is not observed  
460 directly) varies spatially, a statistical distribution for  $A$  is theoretically predicted for each value of  $H$   
which corresponds to the family of predicted curves in  $H$ - $A$  space, Fig. 5a. Additionally, since high  
 $A$  is predicted to be suppressed for high  $H$ , we would expect there to be a statistically lower mean  $A$   
value for the High  $H$  than Low  $H$  category Fig. 7a. In other words; a statistically-distributed inverse  
relationship is predicted.

465 In order to test these predictions, we considered the statistics of the three separate  $A$  distributions  
for each  $H$  category, which are shown for: High  $H$  in Fig. 7b, Medium  $H$  in Fig. 7c, and Low  $H$   
in 7d. These categories correspond to approximately 30 %, 50 % and 20 % of the total data respec-  
tively. A nearest neighbour interpolation was used to pair each  $A$  value ( $\sim$  100-150 m along-track  
spacing) with each  $H$  value (1 km along-track spacing). The lowest mean value, smallest variance,  
470 and strongest positive skew is observed for the High  $H$  category. This supports the general predic-  
tion in Fig. 5 that higher  $A$  values (specular reflections) are suppressed in regions of higher  $H$ , with  
lower  $A$  values (diffuse scattering) being more probable. The highest mean value, greatest variance,  
and weakest positive skew is observed for the Low  $H$  category. This supports the prediction in Fig.  
5 that  $A$  is less constrained in regions of lower  $H$ , with a tendency toward higher values (specu-  
475 lar reflections). As would be expected, the  $A$ -distribution statistics for the Medium  $H$  category lie  
between the High  $H$  and Low  $H$  categories with intermediate mean values, variance, and skewness.

We repeated the above analysis for  $H$  values that were estimated using the variogram for  $\xi(L)$ . The  
distributions for the three  $H$  categories are qualitatively similar to Fig. 7b-d but with less pronounced  
quantitative differences between  $H$  categories (e.g. the mean values for  $A$  are 0.201, 0.243 and 0.254  
480 for High, Medium and Low  $H$  categories respectively). This is as expected, since the length scales  
at which  $H$  is estimated using the devrogram are more directly related to radar scattering than the  
variogram.

### 5.3 Statistics in thawed and frozen regions

The spatial distributions in Fig. 6 indicate that predicted thawed regions of the northern GrIS (using  
485 the basal thermal state mask in Macgregor et al. (2016)) have: higher values of the Hurst exponent,  
higher values of rms deviation (higher topographic-scale roughness), and lower values of waveform  
abruptness (more diffuse scattering), than frozen regions. In order to quantify these observations, we  
considered statistical distributions for thawed/frozen subsets of the along-track data. Distributions  
for  $H$  in thawed/frozen regions (corresponding Fig. 6a) are shown in Fig. 8a and b; distributions for  
490  $\nu(\Delta x=30$  m) in thawed/frozen regions (corresponding to Fig. 6b) are shown in Fig. 8c and d; and  
distributions for  $A$  in thawed/frozen regions (corresponding to Fig. 6d) are shown in Fig. 8e and d.

The distributions for all RES-derived data exhibit pronounced statistical differences between  
thawed and frozen regions. The mean value of  $H$  in thawed regions is 0.74 with a strong nega-  
tive skew, whereas the mean value of  $H$  in frozen regions is 0.54 with a weak negative skew. The



495 mean value of  $\nu(\Delta x=30\text{ m})$  in thawed regions is 6.36 m, which is over double the mean value of  
2.80 m in frozen regions. A qualitatively similar distinction between thawed and frozen regions is  
also present for  $\nu(\Delta x=150\text{ m})$ , with a mean value of 21.7 m in thawed regions and 7.2 m in frozen  
regions (not shown). The thawed distribution for  $A$  is similar to the high  $H$  category in Fig. 7a, with  
a mean  $A$  value of 0.165 and strong positive skew. The frozen distribution is similar to the low  $H$   
500 category in Fig. 7a with a mean  $A$  value of 0.264 and a weak positive skew. An anti-correlation  
between the skewness of the  $H$  and  $A$  distributions is also observed (i.e. in thawed regions a strong  
negative skew for  $H$  is paired with a strong positive skew for  $A$ , and in frozen regions a weak neg-  
ative skew for  $H$  is paired with a weak positive skew for  $A$ ). This provides further observational  
evidence for the applicability of the self-affine radar scattering model (Sect. 4), which predicts a  
505 statistically-distributed inverse relationship between  $H$  and  $A$ .

## 6 Discussion

Our study demonstrates that the Hurst exponent exerts strong topographic control upon the spa-  
tial distribution of the waveform abruptness (radar scattering). Notably, higher values of abruptness  
(specular reflections) are suppressed in regions of higher Hurst exponent, with lower abruptness  
510 (diffuse scattering) being more typical. Additionally, extended continuous regions of higher abrupt-  
ness are generally limited for lower Hurst exponent. Whilst clearly idealised - assuming both radial  
isotropy and a downward extrapolation of  $H$  - the self-affine radar scattering model predicts this  
behaviour, and thus establishes a causative link between the spatial distribution of self-affine rough-  
ness and radar scattering. This finding implies that maps of radar scattering information - including  
515 both the waveform abruptness parameter discussed in here and in Oswald and Gogineni (2008) and  
Oswald and Gogineni (2012), and the specular content in Schroeder et al. (2013) and Young et al.  
(2016) - will, in future, benefit from analysis that takes into account self-affine topographic control.

The waveform abruptness parameter was previously employed by Oswald and Gogineni (2008,  
2012), in the context of basal thaw discrimination. In their algorithm regions of thaw are discrimi-  
520 nated if: (i) the relative reflection coefficient is above a threshold (with reflection defined using the  
aggregated power (see Sect. 3.3), and an attenuation model where the attenuation rate has an in-  
verse relationship with surface elevation); (ii) the abruptness is also above a threshold. Thus, in their  
approach, high abruptness (specular reflections) is a necessary, but not sufficient, criteria for iden-  
tifying basal thaw. Conceptually, their approach assumes that thawed regions have a similar RES  
525 signature to deep (depth > 10 m) subglacial lakes which exhibit brighter and more specular reflec-  
tions than surrounding regions (Oswald and Robin, 1973; Palmer et al., 2013). Shallower (depth <  
10 m) subglacial lakes often produce more diffuse reflections, due to scattering from the lake bot-  
tom and related interference effects Gorman and Siegert (1999). The exact depth at which a lake is



‘shallow’ or ‘deep’, based upon its scattering signature, is dependent on the electrical conductivity,  
530 and 10 m serves as a rough guide (refer to Gorman and Siegert (1999) for a full discussion).

Our statistical analysis of abruptness in predicted frozen and thawed regions (Sect. 5.3) demon-  
strates that, overall, very different RES scattering signatures are likely to be present than were as-  
sumed by Oswald and Gogineni (2008, 2012). Firstly, the majority of the predicted thawed regions  
535 have lower abruptness (associated with diffuse scattering). In their algorithm, this would correspond  
to false-negative detection of basal thaw (since the necessary high abruptness condition for thaw  
is not satisfied). Secondly, high abruptness is often present in predicted frozen regions, many of  
which are interpreted as thawed by Oswald and Gogineni (2008, 2012) (e.g. parts of the region of  
near-continuous higher abruptness around the Camp Century ice core). Since the original work of  
540 Oswald and Gogineni (2008), the role that uncertainty in radar attenuation has in biasing the spa-  
tial distribution of radar reflection has become much better understood (Matsuoka, 2011; Macgregor  
et al., 2012; Jordan et al., 2016). For example, if an attenuation model has a constant systematic bias  
in attenuation rate, then there will be a thickness-correlated bias in estimated basal reflection values  
(Jordan et al., 2016). Thus, it is possible that regions predicted to have high values of relative reflec-  
545 tion in the frozen interior (Oswald and Gogineni, 2008, 2012) do so due to spatially correlated bias  
in the attenuation model. In turn, combined with high abruptness, this would lead to a false-positive  
identification of basal thaw.

It is important to note that both the predictions of the self-affine radar scattering model (Sect. 4),  
and the observed relationship between the abruptness and Hurst exponent (Sect. 5.2), are consistent  
550 with the specular RES scattering signature that we would expect from electrically deep subglacial  
lakes. Under the self-affine roughness framework, a large geometrically flat feature such as a lake  
would have a negligible value of  $H$  and  $\nu_\lambda$ . This scenario occurs for the low  $H$  limit of the green  
curve in Fig. 5a, where predicted values for  $A$  are  $\sim 0.65$  (corresponding to a perfectly specular  
reflection). Whilst the majority of the thawed regions have lower abruptness, there are some smaller,  
localised, patches of higher abruptness present in Fig. 6d: for example, in the main trunk of Pe-  
555 termann glacier ( $80.5^\circ$  N,  $59.5^\circ$  W), and the flight lines just to the North and East of NorthGRIP.  
Whilst these regions are consistent with there being deep water present (in the sense that specular  
reflections are observed in a region predicted to be above pressure melting point), on the basis of the  
RES scattering signature alone it is not possible to confirm that this is the case. This is because the  
frozen abruptness distribution in Fig. 8f indicates that basal water is not required to produce highly  
560 specular reflections, and thus smooth regions of bedrock may be responsible for the high abrupt-  
ness. The presence of at least some localised patches of high abruptness in thawed regions is also  
consistent with the recent discovery of two small subglacial lakes in north western Greenland of  $\sim$   
 $8 \text{ km}^2$  and  $\sim 10 \text{ km}^2$  in extent (Palmer et al., 2013). More generally, however, the relative rarity  
of high abruptness in thawed regions is in agreement with a recent hydrological potential analysis



565 (Livingstone et al., 2013), which predicted that deep subglacial lakes are both rare and small in our region of interest.

The Hurst exponent provides information about the relationship that exists between vertical roughness and the horizontal length scale. Whilst it is related to the slope of the roughness power spectrum, past spectral analysis of glaciological terrain tends to obscure this information (since an integrated  
570 'total roughness' metric is typically used) (Taylor et al., 2004; Siegert et al., 2005; Bingham and Siegert, 2009; Li et al., 2010; Rippin, 2013). Subsequently, the Hurst exponent represents new subglacial roughness information, that could potentially be utilised much more widely than our current application in constraining radar scattering. For example, planetary scientists have previously employed the Hurst exponent in a geostatistical classification of Martian terrain (Orosei et al., 2003).  
575 Interestingly, the spatial distribution of the Hurst exponent for the Martian surface, has a similar level of spatial variation and coherence to what we observe for glacial terrain. Additionally, the distribution of  $H$  for Martian terrain is skewed toward higher, self-similar, values with near-continuous regions of lower  $H$  limited to mid-latitude plains. For Greenland, this self-affine statistical landscape classification could be integrated with existing knowledge of geology (e.g. Henriksen (2008)) and  
580 preglacial landscape features; including paleofluvial drainage networks (Cooper et al., 2016) and paleofluvial canyons (Bamber et al., 2013b).

Whilst topographic (spectral) roughness analysis has already been performed for topography beneath ice sheets (e.g. for the Greenland Ice Sheet by Rippin (2013), and the East Antarctica Ice Sheet by Siegert et al. (2005)), analysis is limited to a horizontal length scale that is greater than the along-track resolution (typically  $\sim 30$  m or greater). This minimum observable length scale is significantly  
585 greater than the dominant (metre) length scale at which the processes that modulate basal sliding - enhanced plastic flow and relegation - operate at (Weertman, 1957; Nye, 1970; Hubbard et al., 2000; Fowler, 2011). The maps for topographic-scale rms deviation in Fig. 6b and c, and related analysis in Sect. 5.3, both demonstrate that rougher terrain at the topographic scale occurs in thawed regions  
590 rather than frozen regions. This is the opposite behaviour to what we would expect if the roughness measure plays a direct role in modulating basal sliding, confirming the view that the length-scale is likely to be too large to be relevant. Since it is formulated with respect to wavelength (approximately metre) scale roughness, the self-affine radar scattering model, provides a way to estimate metre-scale roughness (i.e. given  $A$  and  $H$  obtain an estimate for  $\nu_\lambda$  in accordance with the curves in Fig. 5).  
595 There is an obvious caveat, however, that the basal roughness parameters used in this study - rms height and rms deviation - are chosen because they enable the parameterisation of radar scattering (not for their direct relevance to basal sliding physics). Therefore, as is being explored in other recent subglacial roughness works (Li et al., 2010; Rippin et al., 2014; Wilkens et al., 2015), these radar roughness parameters could potentially be modified for glaciological application.

600 The Hurst exponent has previously been shown to play a dynamical role in the flow resistance of alluvial channels (Robert, 1988). Whilst basal sliding is clearly a different physical phenomena, it is



possible that the Hurst exponent itself may provide a useful radar-derived parameter for informing our understanding of geometric control upon this process. In Sect. 5.1 and Sect. 5.3 we observed that predicted thawed regions of the glacial bed are characterised by higher (often near self-similar) values of the Hurst exponent, whereas frozen regions are characterised by lower values (normally Brownian, or sub-Brownian). One could therefore conjecture that the persistent behaviour (neighbouring points follow similar elevation trend) associated with high  $H$  interfaces (see Sect. 2.3) could act to promote basal sliding, whereas the anti-persistent behaviour (neighboring points alternate in elevation trend) associated with low  $H$  interfaces could act to inhibit basal sliding. However, as is widely acknowledged, attributing a direct link between subglacial roughness and contemporary ice dynamics is a complex topic (Siegert et al., 2005; Bingham and Siegert, 2009; Rippin et al., 2014). Therefore, as with other measures or basal roughness, the spatial variation in the Hurst exponent is likely to both originate from, and influence, different glaciological processes at a variety of spatial scales. Additionally, we recommend that future works which investigate the connection between the Hurst exponent and glaciological processes should be discussed with reference to anisotropy (in particular with respect to the flow direction).

The pronounced spatial heterogeneity of  $H$  implies that estimation of roughness statistics from  $H=0$  radar scattering models (Eq. (9) and (Berry, 1973; Ulaby et al., 1982; Peters et al., 2005; Grima et al., 2014)) may give erroneous results; particularly when comparing the overall spatial distribution between regions with different  $H$  values. We did not consider the anisotropy of the Hurst exponent in our radar scattering model, which was justifiable because we were interested in understanding how the Hurst exponent relates to the (near) isotropic abruptness. However, in certain regions of the ice sheets, basal radar scattering is known to be highly anisotropic; as revealed by maps of the specular content for Thwaites glacier by Schroeder et al. (2013) and Byrd Glacier by Young et al. (2016). Thus a clear direction of future research would be to modify the self-affine radar scattering model (Sect. 4) to take into account anisotropy in  $H$ , and then to compare this model with maps for the specular content.

Finally, geostatistically-based interpolation methods which employ aspects of self-affine statistics (Goff and Jordan, 1988), have found recent application in generating synthetic subglacial topography (Goff et al., 2014). The self-affine characterisation of subglacial topography described here informs such techniques, and, in turn, could be used to inform the ice-sheet-wide interpolation of future Greenland (Bamber et al., 2013a) and Antarctic (Fretwell et al., 2013) subglacial digital elevation maps.

## 7 Summary and conclusions

In this study we used recent OIB RES data to demonstrate that subglacial roughness in northern Greenland exhibits self-affine scaling behaviour, with pronounced spatial variation in the Hurst



(roughness power-law) exponent. We used a self-affine radar scattering model to predict how the Hurst exponent exerts control upon the spatial distribution of radar scattering, which we quantified using the waveform abruptness parameter. We then demonstrated a general agreement between the  
640 predictions of the radar scattering model and the observed relationship between the Hurst exponent and waveform abruptness. Notably, high values of abruptness (specular reflections) are suppressed in regions of higher Hurst exponent, with continuous higher abruptness generally occurring in regions with a lower Hurst exponent. This agreement between predictions and observations enables us to conclude that self-affine roughness statistics provide a valuable framework in understanding the  
645 topographic control which influences radar scattering.

A central glaciological motivation behind our study was to establish if the waveform abruptness could be used to aid in the discrimination of thawed beds (under the initial assumption that thawed beds produce specular reflections). To do this we compared our RES-derived data fields with a predicted thermal state mask for northern Greenland. The analysis demonstrated that thawed regions  
650 of the glacier bed have statistically lower values of the waveform abruptness than frozen regions. Hence, whilst high reflection specularity is a typical RES signature of subglacial lakes, it is not a typical RES signature of thawed regions of the Greenlandic subglacial interface. We therefore conclude that RES methods which seek to discriminate thawed regions, as distinct from deep (> 10 m) subglacial lakes or other electrically deep water bodies, should not use high waveform abruptness  
655 (high reflection specularity) as a necessary criteria for discrimination of a thawed bed.

*Acknowledgements.* T.M.J., J.L.B., and C.N.W. were supported by UK NERC grant NE/M000869/1 as part of the Basal Properties of Greenland project. M.A.C. was supported by the UK NERC grant NE/L002434/1 as part of the NERC Great Western Four + (GW4+) Doctoral Training Partnership. We would like to thank J.A. Macgregor, NASA Goddard Space Flight Center, USA, for kindly supplying the Greenland thermal state mask.



## 660 References

- Bamber, J. L., Griggs, J. A., Hurkmans, R. T. W. L., Dowdeswell, J. A., Gogineni, S. P., Howat, I., Mouginot, J., Paden, J., Palmer, S., Rignot, E., and Steinhage, D.: A new bed elevation dataset for Greenland, *The Cryosphere*, 7, 499–510, doi:10.5194/tc-7-499-2013, 2013a.
- Bamber, J. L., Siegert, M. J., Griggs, J. A., Marshall, S. J., and Spada, G.: Paleofluvial Mega-Canyon Beneath  
665 the Central Greenland Ice Sheet, *Science*, 341, 997–1000, doi:10.1126/science.1239794, 2013b.
- Berry, M. V.: The Statistical Properties of Echoes Diffracted from Rough Surfaces, *Philosophical Transactions of the Royal Society A: Mathematical, Physical and Engineering Sciences*, 273, 611–654, doi:10.1098/rsta.1973.0019, 1973.
- Bingham, R. G. and Siegert, M. J.: Quantifying subglacial bed roughness in Antarctica: implications for ice-  
670 sheet dynamics and history, *Quaternary Science Reviews*, 28, 223–236, doi:10.1016/j.quascirev.2008.10.014, 2009.
- Bogorodsky, V. R., Bentley, C. R., and Gudmundsen, P. E.: *Radioglaciology*, chap. 6, p. 216, D. Reidel Publishing Company, 1983.
- Campbell, B. A. and Shepard, M. K.: Coherent and incoherent components in near-nadir radar scattering: Applications to radar sounding of Mars, *Journal of Geophysical Research*, 108, 1–8, doi:10.1029/2003JE002164, 2003.
- Cooper, M. A., Michaelides, K., Siegert, M. J., and Bamber, J. L.: Paleofluvial landscape inheritance for Jakobshavn Isbræ catchment, Greenland, *Geophysical Research Letters*, 43, 6350–6357, doi:10.1002/2016GL069458, 2016.
- 680 Cornford, S. L., Martin, D. F., Payne, A. J., Ng, E. G., Le Brocq, A. M., Gladstone, R. M., Edwards, T. L., Shannon, S. R., Agosta, C., van den Broeke, M. R., Hellmer, H. H., Krinner, G., Ligtenberg, S. R. M., Timmermann, R., and Vaughan, D. G.: Century-scale simulations of the response of the West Antarctic Ice Sheet to a warming climate, *The Cryosphere*, 9, 1887–1942, doi:10.5194/tcd-9-1887-2015, 2015.
- Fowler, A. C.: Weertman, Llibouty and the development of sliding theory, *Journal of Glaciology*, 56, 965–972,  
685 doi:10.3189/002214311796406112, 2011.
- Franceschetti, G., Iodice, A., Member, S., Migliaccio, M., Riccio, D., and Member, S.: Scattering from Natural Rough Surfaces Modeled by Fractional Brownian Motion Two-Dimensional Processes, *IEEE Transactions on Antennas and Propagation*, 47, 1405–1415, doi:10.1109/8.793320, 1999.
- Fretwell, P., Pritchard, H. D., Vaughan, D. G., Bamber, J. L., Barrand, N. E., Bell, R., Bianchi, C., Bingham, R. G., Blankenship, D. D., Casassa, G., Catania, G., Callens, D., Conway, H., Cook, A. J., Corr, H. F. J., Damaske, D., Damm, V., Ferraccioli, F., Forsberg, R., Fujita, S., Gim, Y., Gogineni, P., Griggs, J. A., Hindmarsh, R. C. A., Holmlund, P., Holt, J. W., Jacobel, R. W., Jenkins, A., Jokat, W., Jordan, T., King, E. C., Kohler, J., Krabill, W., Riger-Kusk, M., Langley, K. A., Leitchenkov, G., Leuschen, C., Luyendyk, B. P., Matsuoka, K., Mouginot, J., Nitsche, F. O., Nogi, Y., Nost, O. A., Popov, S. V., Rignot, E., Rippin, D. M.,  
695 Rivera, A., Roberts, J., Ross, N., Siegert, M. J., Smith, A. M., Steinhage, D., Studinger, M., Sun, B., Tinto, B. K., Welch, B. C., Wilson, D., Young, D. A., Xiangbin, C., and Zirizzotti, A.: Bedmap2: Improved ice bed, surface and thickness datasets for Antarctica, *The Cryosphere*, 7, 375–393, doi:10.5194/tc-7-375-2013, 2013.



- Fujita, S., Holmlund, P., Matsuoka, K., Enomoto, H., Fukui, K., Nakazawa, F., Sugiyama, S., and Surdyk, S.:  
700 Radar diagnosis of the subglacial conditions in Dronning Maud Land, East Antarctica, *The Cryosphere*, 6,  
1203–1219, doi:10.5194/tc-6-1203-2012, 2012.
- Goff, J. A. and Jordan, T. H.: Stochastic modeling of seafloor morphology: Inversion of Sea  
Beam data for Second-Order Statistics, *Journal of Geophysical Research*, 93, 13 589–13 608,  
doi:10.1029/JB093iB11p13589, 1988.
- 705 Goff, J. A., Powell, E. M., Young, D. A., and Blankenship, D. D.: Instruments and Methods Conditional sim-  
ulation of Thwaites Glacier (Antarctica) bed topography for flow models: incorporating inhomogeneous  
statistics and channelized morphology, *Journal of Glaciology*, 60, 635–646, doi:10.3189/2014JoG13J200,  
2014.
- Gogineni, S., Yan, J.-B., Paden, J., Leuschen, C., Li, J., Rodriguez-Morales, Braaten, D., Purdon, K., Wang,  
710 Z., Liu, W., and Gauch, J.: Bed topography of Jakobshavn Isbrae, Greenland, and Byrd Glacier, Antarctica,  
*Journal of Glaciology*, 60, 813–833, doi:10.3189/2014JoG14J129, 2014.
- Gorman, M. R. and Siegert, M. J.: Penetration of Antarctic subglacial lakes by VHF electromagnetic pulses:  
Information on the depth and electrical conductivity of basal water bodies, *Journal of Geophysical Research*,  
104, 29 311–29 320, 1999.
- 715 Grima, C., Schroeder, D. M., Blankenship, D. D., and Young, D. A.: Planetary landing-zone reconnaissance  
using ice-penetrating radar data: Concept validation in Antarctica, *Planetary and Space Science*, 103, 191–  
204, doi:10.1016/j.pss.2014.07.018, 2014.
- Henriksen, N.: Geological History of Greenland. Four Billion Years of Earths Evolution, vol. 1st edition, Geo-  
logical Survey of Greenland and Denmark, (GEUS), 2008.
- 720 Hubbard, B., Siegert, M. J., and McCarroll, D.: Spectral roughness of glaciated bedrock geomorphic surfaces:  
implications for glacier sliding, *Journal of Geophysical Research*, 105, 21 295, doi:10.1029/2000JB900162,  
2000.
- Jacobel, R. W., Welch, B. C., Osterhouse, D., Pettersson, R., and Macgregor, J. A. M.: Spatial variation of radar-  
derived basal conditions on Kamb Ice Stream, West Antarctica, *Annals of Glaciology*, 50, 10–16, 2009.
- 725 Jordan, T. M., Bamber, J. L., Williams, C. N., Paden, J. D., Siegert, M. J., Huybrechts, P., Gagliardini, O., and  
Gillet-Chaulet, F.: An ice-sheet-wide framework for englacial attenuation from ice-penetrating radar data,  
*The Cryosphere*, 10, 1547–1570, doi:10.5194/tc-10-1547-2016, 2016.
- Kulatilake, P., Um, J., and Pan, G.: Requirements for accurate quantification of self-affine roughness using the  
variogram method, *Int. J. Solids Structures*, 35, 4167–4189, doi:10.1016/S0020-7683(97)00308-9, 1998.
- 730 Li, X., Sun, B., Siegert, M. J., Bingham, R. G., Tang, X., Zhang, D., Cui, X., and Zhang, X.: Characteri-  
zation of subglacial landscapes by a two-parameter roughness index, *Journal of Glaciology*, 56, 831–836,  
doi:10.3189/002214310794457326, 2010.
- Livingstone, S. J., Clark, C. D., Woodward, J., and Kingslake, J.: Potential subglacial lake locations and melt-  
water drainage pathways beneath the Antarctic and Greenland ice sheets, *The Cryosphere*, 7, 1721–1740,  
735 doi:10.5194/tc-7-1721-2013, 2013.
- Macgregor, J. A., Matsuoka, K., Waddington, E. D., Winebrenner, D. P., and Pattyn, F.: Spatial variation of  
englacial radar attenuation: Modeling approach and application to the Vostok flowline, *Journal of Geophys-  
ical Research*, 117, F03 022, doi:10.1029/2011JF002327, 2012.



- Macgregor, J. A., Catania, G. A., Conway, H., Schroeder, D. M., Joughin, I., Young, D. A., Kempf, S. D., and  
740 Blankenship, D. D.: Weak bed control of the eastern shear margin of Thwaites Glacier, West Antarctica,  
*Journal of Glaciology*, 59, 900–912, doi:10.3189/2013JoG13J050, 2013.
- Macgregor, J. A., Li, J., Paden, J. D., Catania, G. A., and Clow, G. D.: Radar attenuation and tempera-  
ture within the Greenland Ice Sheet, *Journal of Geophysical Research: Earth Surface*, 120, 983–1008,  
doi:10.1002/2014JF003418, 2015.
- 745 Macgregor, J. A., Fahnestock, M. A., Catania, G. A., Aschwanden, A., Clow, G. D., Colgan, W. T., Gogineni,  
S. P., Morlighem, M., Nowicki, S. M. J., Paden, J. D., Price, S. F., and Seroussi, H.: A synthesis of the basal  
thermal state of the Greenland ice sheet, *Journal of Geophysical Research: Earth Surface*, 127, 1328–1350,  
doi:10.1002/2015JF003803, 2016.
- Malinverno, A.: A simple method to estimate the fractal dimension of self-affine series, *Geophysical Research*  
750 *Letters*, 17, 1953–1956, 1990.
- Matsuoka, K.: Pitfalls in radar diagnosis of ice-sheet bed conditions: Lessons from englacial attenuation models,  
*Geophysical Research Letters*, 38, 1–5, doi:10.1029/2010GL046205, 2011.
- Matsuoka, K., MacGregor, J. A., and Pattyn, F.: Predicting radar attenuation within the Antarctic ice sheet,  
*Earth and Planetary Science Letters*, 359–360, 173–183, doi:10.1016/j.epsl.2012.10.018, 2012.
- 755 Morris, A. R., Anderson, F. S., Mouginiis-mark, P. J., Haldemann, A. F. C., Brooks, B. A., and Foster, J.: Rough-  
ness of Hawaiian volcanic terrains, *Journal of Geophysical Research*, 113, 1–20, doi:10.1029/2008JE003079,  
2008.
- Nowicki, S., Bindschadler, R. A., Abe-Ouchi, A., Aschwanden, A., Bueller, E., Choi, H., Fastook, J., Granzow,  
G., Greve, R., Gutowski, G., Herzfeld, U., Jackson, C., Johnson, J., Khroulev, C., Larour, E., Levermann, A.,  
760 Lipscomb, W. H., Martin, M. A., Morlighem, M., Parizek, B. R., Pollard, D., Price, S. F., Ren, D., Rignot, E.,  
Saito, F., Sato, T., Seddik, H., Seroussi, H., Takahashi, K., Walker, R., and Wang, W. L.: Insights into spatial  
sensitivities of ice mass response to environmental change from the SeaRISE ice sheet modeling project II:  
Greenland, *Journal of Geophysical Research: Earth Surface*, 118, 1025–1044, doi:10.1002/jgrf.20076, 2013.
- Nye, J. F.: Glacier sliding without cavitation in a linear viscous approximation, *Proc. Roy. Soc. Lond. A.*, 315,  
765 381–403, doi:10.1098/rspa.1983.0054, 1970.
- Oleschko, K., Korvin, G., Figueroa, B., Vuelvas, M. A., Balankin, A. S., Flores, L., and Carreo, D.: Fractal  
radar scattering from soil, *Physical Review E*, 67, 041 403, doi:10.1103/PhysRevE.67.041403, 2003.
- Orosei, R., Bianchi, R., Coradini, A., Espinasse, S., Federico, C., Ferriccioni, A., and Gavrishin, A. I.: Self-  
affine behavior of Martian topography at kilometer scale from Mars Orbiter Laser Altimeter data, *Journal of*  
770 *Geophysical Research*, 108, 1–10, doi:10.1029/2002JE001883, 2003.
- Oswald, G. and Gogineni, S.: Recovery of subglacial water extent from Greenland radar survey data, *Journal of*  
*Glaciology*, 54, 94–106, doi:10.3189/002214308784409107, 2008.
- Oswald, G. K. A. and Gogineni, S. P.: Mapping Basal Melt Under the Northern Greenland Ice Sheet, *IEEE*  
*Transactions on Geoscience and Remote Sensing*, 50, 585–592, doi:10.1109/TGRS.2011.2162072, 2012.
- 775 Oswald, G. K. A. and Robin, G. D. Q.: Lakes Beneath the Antarctic Ice Sheet, *Nature*, 245, 251–254,  
doi:10.1038/245251a0, 1973.
- Paden, J.: Radar Depth Sounder, Centre for Remote Sensings of Ice Sheets, [http://data.cresis.ku.edu/data/rds/  
rds\\_readme.pdf](http://data.cresis.ku.edu/data/rds/rds_readme.pdf), [last access: Dec 2015], 2015.



- Palmer, S. J., Dowdeswell, J. A., Christoffersen, P., Young, D. A., Blankenship, D. D., Greenbaum, J. S., Ben-  
780 ham, T., Bamber, J., and Siegert, M. J.: Greenland subglacial lakes detected by radar, *Geophysical Research  
Letters*, 40, 6154–6159, doi:10.1002/2013GL058383, 2013.
- Peacock, N. R. and Laxon, S. W.: Sea surface height determination in the Arctic Ocean from ERS altimetry,  
*Journal of Geophysical Research*, 109, C07 001, doi:10.1029/2001JC001026, 2004.
- Peters, M. E., Blankenship, D. D., and Morse, D. L.: Analysis techniques for coherent airborne radar  
785 sounding: Application to West Antarctic ice streams, *Journal of Geophysical Research*, 110, B06 303,  
doi:10.1029/2004JB003222, 2005.
- Price, S. F., Payne, A. J., Howat, I. M., and Smith, B. E.: Committed sea-level rise for the next century from  
Greenland ice sheet dynamics during the past decade., *Proceedings of the National Academy of Sciences of  
the United States of America*, 108, 8978–83, doi:10.1073/pnas.1017313108, 2011.
- 790 Pritchard, H. D.: Bedgap: where next for Antarctic subglacial mapping?, *Antarctic Science*, 26, 742–757,  
doi:10.1017/S095410201400025X, 2014.
- Rippin, D. M.: Bed roughness beneath the Greenland ice sheet, *Journal of Glaciology*, 59, 724–732,  
doi:10.3189/2013JoG12J212, 2013.
- Rippin, D. M., Bingham, R. G., Jordan, T. A., Wright, A. P., Ross, N., Corr, H. F. J., Ferraccioli, F.,  
795 Le Brocq, A. M., Rose, K. C., and Siegert, M. J.: Basal roughness of the Institute and Möller Ice  
Streams, West Antarctica: Process determination and landscape interpretation, *Geomorphology*, 214, 139–  
147, doi:10.1016/j.geomorph.2014.01.021, 2014.
- Ritz, C., Edwards, T. L., Durand, G., Payne, A. J., Peyaud, V., and Hindmarsh, R. C. A.: Potential  
sea-level rise from Antarctic ice-sheet instability constrained by observations, *Nature*, 528, 115–118,  
800 doi:10.1038/nature16147, 2015.
- Robert, A.: Statistical Properties of Sediment Bed Profiles in Alluvial Channels, *Mathematical Geology*, 20,  
205–225, doi:10.1007/BF00890254, 1988.
- Rodriguez-Morales, F., Gogineni, S., Leuschen, C. J., Paden, J. D., Li, J., Lewis, C. C., Panzer, B., Gomez-  
Garcia Alvestegui, D., Patel, A., Byers, K., Crowe, R., Player, K., Hale, R. D., Arnold, E. J., Smith, L., Gif-  
805 ford, C. M., Braaten, D., and Panton, C.: Advanced multifrequency radar instrumentation for polar Research,  
*IEEE Transactions on Geoscience and Remote Sensing*, 52, 2824–2842, doi:10.1109/TGRS.2013.2266415,  
2014.
- Schroeder, D. M., Blankenship, D. D., and Young, D. A.: Evidence for a water system transition beneath  
Thwaites Glacier, West Antarctica., *Proceedings of the National Academy of Sciences of the United States  
810 of America*, 110, 12 225–8, doi:10.1073/pnas.1302828110, 2013.
- Schroeder, D. M., Blankenship, D. D., Young, D. A., Witus, A. E., and Anderson, J. B.: Airborne radar sounding  
evidence for deformable sediments and outcropping bedrock beneath Thwaites Glacier, West Antarctica,  
*Geophysical Research Letters*, pp. 7200–7208, doi:10.1002/2014GL061645, 2014.
- Schroeder, D. M., Blankenship, D. D., Raney, R. K., and Grima, C.: Estimating Subglacial Water Geometry  
815 Using Radar Bed Echo Specularity : Application, *IEEE Geoscience and Remote Sensing Letters*, 12, 443–  
447, doi:10.1109/LGRS.2014.2337878, 2015.



- Schroeder, D. M., Grima, C., and Blankenship, D. D.: Evidence for variable grounding-zone and shear-margin basal conditions across Thwaites Glacier, West Antarctica, *Geophysics*, 81, WA35–WA43, doi:10.1190/geo2015-0122.1, 2016.
- 820 Sergienko, O. V., Creyts, T. T., and Hindmarsh, R. C. A.: Similarity of organized patterns in driving and basal stresses of Antarctic and Greenland ice sheets beneath extensive, *Geophysical Research Letters*, pp. 3925–3932, doi:10.1002/2014GL059976, 2014.
- Seroussi, H., Morlighem, M., Rignot, E., Khazendar, A., Larour, E., and Mouginot, J.: Dependence of century-scale projections of the Greenland ice sheet on its thermal regime, *Journal of Glaciology*, 59, 1024–1034, doi:10.3189/2013JG13J054, 2013.
- 825 Shannon, S. R., Payne, A. J., Bartholomew, I. D., van den Broeke, M. R., Edwards, T. L., Fettweis, X., Gagliardini, O., Gillet-Chaulet, F., Goelzer, H., Hoffman, M. J., Huybrechts, P., Mair, D. W. F., Nienow, P. W., Perego, M., Price, S. F., Smeets, C. J. P. P., Sole, A. J., van de Wal, R. S. W., and Zwinger, T.: Enhanced basal lubrication and the contribution of the Greenland ice sheet to future sea-level rise., *Proceedings of the National Academy of Sciences of the United States of America*, 110, 14 156–61, doi:10.1073/pnas.1212647110, 2013.
- 830 Shepard, M. K. and Campbell, B. A.: Radar Scattering from a Self-Affine Fractal Surface: Near-Nadir Regime, *Icarus*, 141, 156–171, doi:10.1006/icar.1999.6141, 1999.
- Shepard, M. K., Brackett, R. A., and Arvidson, R. E.: Self-affine (fractal) topography: Surface parameterization and radar scattering, *Journal of Geophysical Research*, 100, 709–718, doi:10.1029/95JE00664, 1995.
- 835 Shepard, M. K., Campbell, B. A., Bulmer, M. H., Farr, T. G., Gaddis, L. R., and Plaut, J. J.: The roughness of natural terrain: A planetary and remote sensing perspective, *Journal of Geophysical Research*, 106, 32 777–32 795, doi:10.1029/2000JE001429, 2001.
- Siegert, M. J., Taylor, J., and Payne, A. J.: Spectral roughness of subglacial topography and implications for former ice-sheet dynamics in East Antarctica, *Global and Planetary Change*, 45, 249–263, doi:10.1016/j.gloplacha.2004.09.008, 2005.
- 840 Smith, M. W.: Roughness in the Earth Sciences, *Earth-Science Reviews*, 136, 202–225, doi:10.1016/j.earscirev.2014.05.016, 2014.
- Taylor, J., Siegert, M. J., Payne, A. J., and Hubbard, B.: Regional-scale bed roughness beneath ice masses: Measurement and analysis, *Computers and Geosciences*, 30, 899–908, doi:10.1016/j.cageo.2004.06.007, 2004.
- 845 Turcotte, D. L.: *Fractals and Chaos in Geology and Geophysics*, Cambridge University Press, New York, 1992.
- Ulaby, F. T., Moore, R. K., and Fung, A. K.: *Microwave Remote Sensing Active and Passive*, vol. 2, chap. Radar Remote Sensing and Surface Scattering and Emission Theory, Addison-Wesley-Longman, 1982.
- Weertman, J.: On the sliding of glaciers, *Journal of Glaciology*, 3, 33–38, doi:10.1007/978-94-015-8705-1\_19, 1957.
- 850 Wilkens, N., Behrens, J., Kleiner, T., Rippin, D., Rückamp, M., and Humbert, A.: Thermal structure and basal sliding parametrisation at Pine Island Glacier - A 3-D full-Stokes model study, *The Cryosphere*, 9, 675–690, doi:10.5194/tc-9-675-2015, 2015.
- Wolovick, M. J., Bell, R. E., Creyts, T. T., and Frearson, N.: Identification and control of subglacial water networks under Dome A, Antarctica, *Journal of Geophysical Research*, 118, 140–154, doi:10.1029/2012JF002555, 2013.
- 855



Young, D. A., Schroeder, D. M., Blankenship, D. D., Kempf, S. D., and Quartini, E.: The distribution of basal water between Antarctic subglacial lakes from radar sounding, *Phil. Trans. R. Soc. A.*, 374, doi:10.1098/rsta.2014.0297, 2016.

860 Zyguntowska, M., Khvorostovsky, K., Helm, V., and Sandven, S.: Waveform classification of airborne synthetic aperture radar altimeter over Arctic sea ice, *The Cryosphere*, 7, 1315–1324, doi:10.5194/tc-7-1315-2013, 2013.

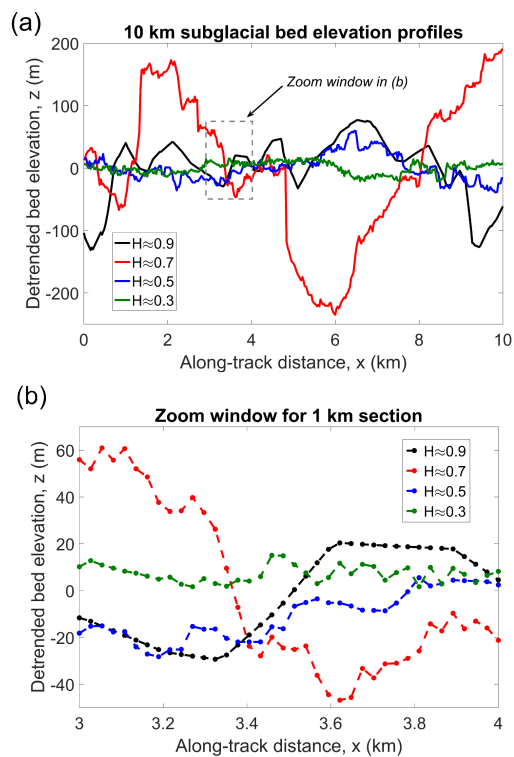


**Figure 1.** Examples of along-track bed elevation profiles for subglacial terrain with different Hurst exponent,  $H$ . (a) 10 km profile window. (b) Zoom to 1 km window with sample points indicated (corresponding to  $\sim 30$  m along-track resolution). The bed elevation is linearly detrended for each 10 km window. The aspect ratio differs between subplots.

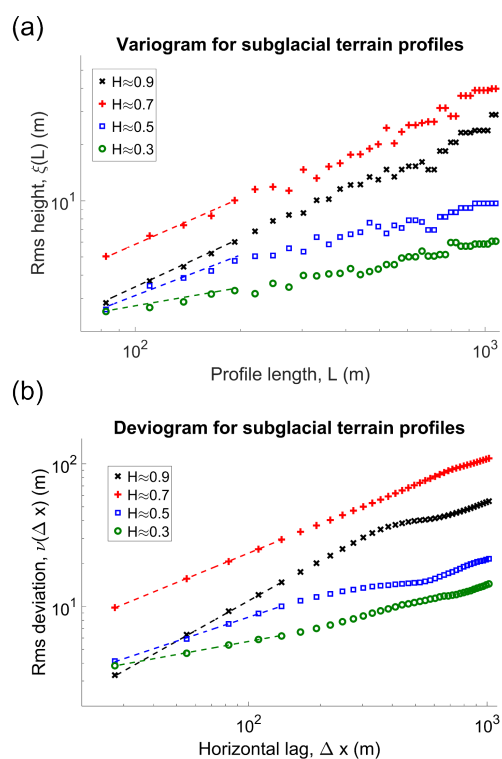


**Figure 2.** (a) Variogram for rms height,  $\xi$ , versus profile length  $L$  (log-log scale). (b) Deviogram for rms deviation,  $\nu$ , versus horizontal lag,  $\Delta x$  (log-log scale). The plots correspond to subglacial terrain profiles in Fig. 1a. The Hurst exponent is estimated from the linear gradient of the first five data points (indicated by dashed lines). These space-domain plots are (approximate) equivalents to frequency-domain roughness power spectra, and smaller length-scales correspond to higher frequencies.

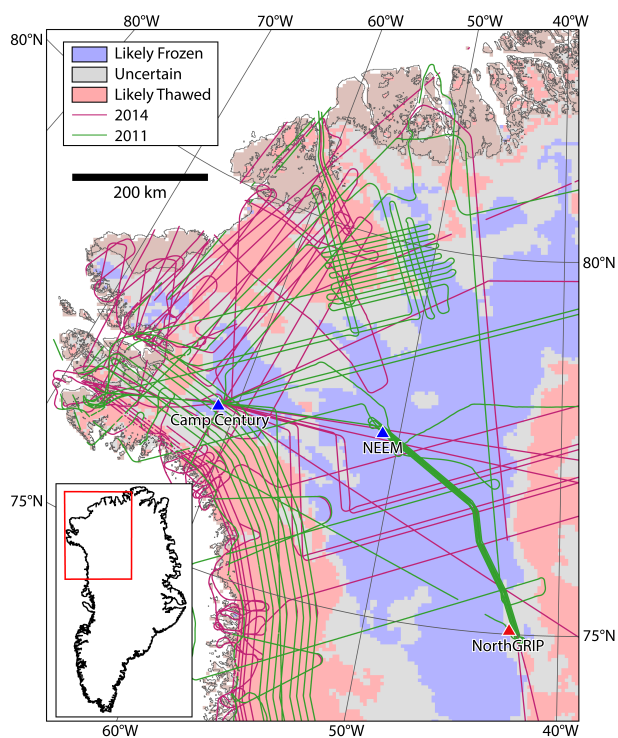


**Figure 3.** Data coverage map for OIB flight lines and region of interest. The map is underlain by the thermal state mask in Macgregor et al. (2016) where red, blue and grey colours correspond to predicted thawed, frozen and uncertain regions of the glacier bed. The locations of the Camp Century, NEEM and NorthGRIP ice cores are indicated.

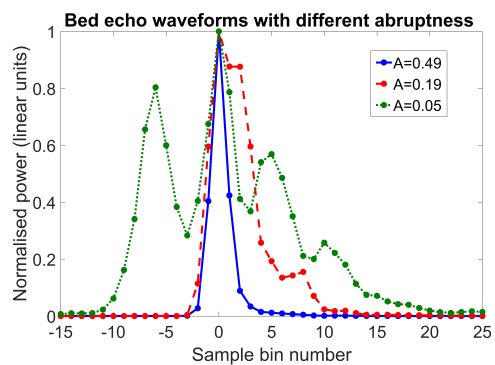


**Figure 4.** Examples of bed echo waveforms and their abruptness (pulse peakiness). Observed values for  $A$  range from  $\sim 0.03$  (associated with diffuse scattering) to  $\sim 0.60$  (associated with specular reflection). For the purpose of comparative plotting, the waveforms are normalised about their peak power values with the sample bin of the peak power set to zero. The sample bin spacing corresponds to a depth-range spacing of  $\sim 2.81$  m.

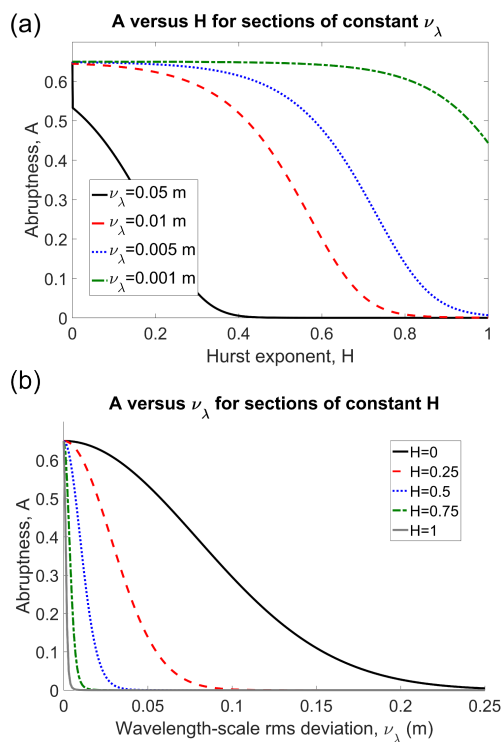


**Figure 5.** Parametric dependence of the self-affine radar scattering model. (a) Abruptness,  $A$ , as a function of the Hurst exponent,  $H$ , for sections of constant wavelength scale rms deviation,  $\nu_\lambda$ . (b)  $A$  as a function of  $\nu_\lambda$  for sections of constant  $H$ . The plots illustrate primary dependence for  $A$  upon  $H$ , and secondary dependence for  $A$  upon  $\nu_\lambda$ . High  $A$  is suppressed for high  $H$ , except in the case of exceptionally small  $\nu_\lambda$ .

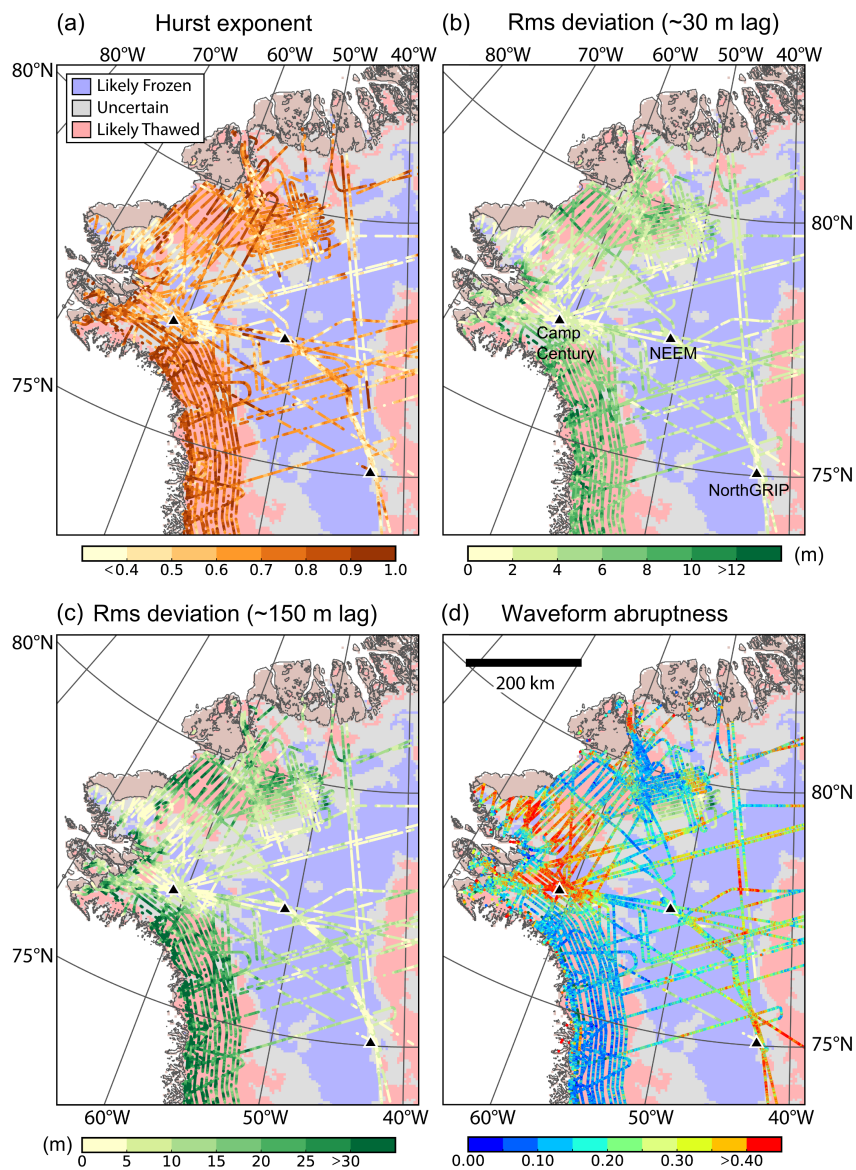


**Figure 6.** Data maps for basal RES analysis in the northern GrIS. (a) Hurst exponent,  $H$ . (b) Rms deviation (topographic roughness) at  $\sim 30$  m lag,  $\nu(\Delta x=30 \text{ m})$ . (c) Rms deviation at  $\sim 150$  m lag,  $\nu(\Delta x=150 \text{ m})$ . (d) Waveform abruptness (radar scattering),  $A$ . The maps are underlain by the predicted thermal state mask in Macgregor et al. (2016) where red, blue and grey colours correspond to predicted thawed, frozen and uncertain regions of the glacier bed. Higher values of  $A$  in (d) indicate more specular reflections.

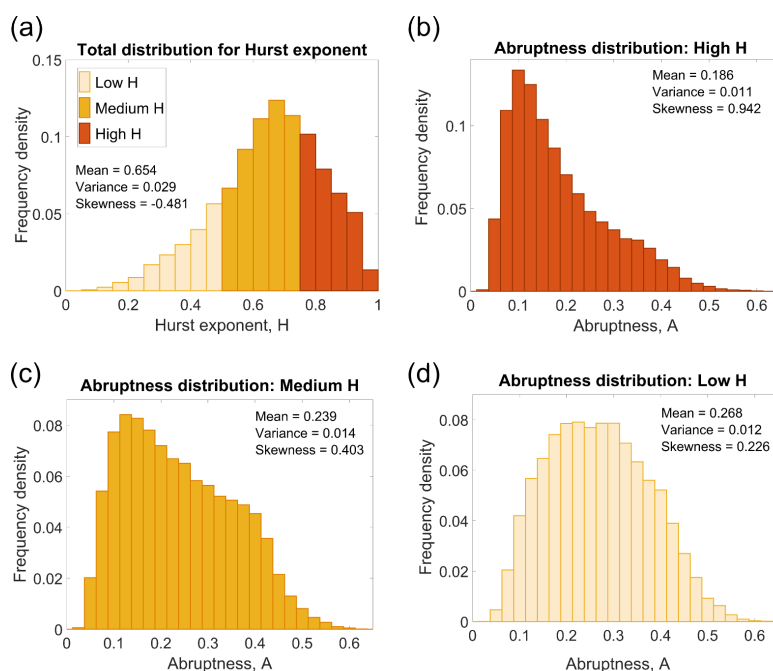


**Figure 7.** Relationship between Hurst exponent,  $H$ , and waveform abruptness,  $A$ . (a) Total distribution for Hurst exponent (corresponding to data in Fig. 6a). (b) Abruptness distribution for  $H > 0.75$  ('High  $H$ '). (c) Abruptness distribution for  $0.5 < H \leq 0.75$ , ('Medium  $H$ '). (d) Abruptness distribution for  $H \leq 0.5$  ('Low  $H$ '). The observed distributions in (b), (c) and (d) confirm the theoretical prediction of the self-affine radar scattering model that a statistically-distributed inverse relationship exists between  $H$  and  $A$ . The analysis is performed independent of the thawed-frozen statistics in Sect. 5.3.

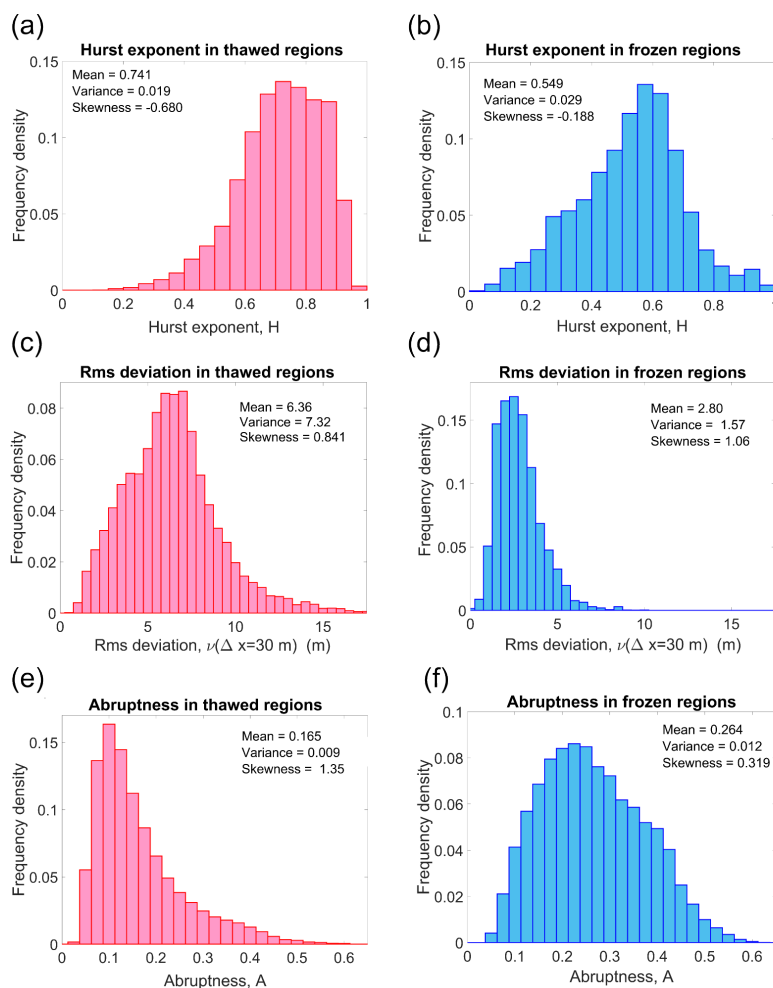


**Figure 8.** Distributions from basal RES analysis in thawed and frozen regions of the northern GrIS. (a) Hurst exponent,  $H$ , in thawed regions, (b)  $H$  in frozen regions. (c) Rms deviation,  $\nu(\Delta x=30 \text{ m})$ , in thawed regions. (d)  $\nu(\Delta x=30 \text{ m})$  in frozen regions. (e) Abruptness,  $A$ , in thawed regions. (f)  $A$  in frozen regions. The data subsets correspond to the red (thawed) and blue (frozen) regions of the maps in Fig. 6.